Journal of Materials Chemistry A

ROYAL SOCIETY OF CHEMISTRY

PAPER

View Article Online
View Journal | View Issue

Cite this: *J. Mater. Chem. A*, 2021, **9**, 1006

Vacancy cluster-induced local disordered structure for the enhancement of thermoelectric property in $Cu_2ZnSnSe_4$†

Zhou Li,[a] Weihui Zhang,[b] Bingchuan Gu,[c] Chenxi Zhao,[b] Bangjiao Ye,[c] Chong Xiao *[ab] and Yi Xie [ab]

Received 9th October 2020
Accepted 30th November 2020

DOI: 10.1039/d0ta09866c

rsc.li/materials-a

Low thermal conductivity is commonly seen in amorphous or disordered systems, in which electrical conductivity is also very low, bringing considerable obstacles to the development of high-performance thermoelectric materials. Present study highlights the vacancy cluster-induced local disordered structure in $Cu_2ZnSnSe_4$ for the simultaneous achievement of low thermal conductivity and high electrical conductivity, thereby significantly enhancing its thermoelectric property. Comprehensive evidences from positron annihilation and HRTEM characterizations indicated that the vacancies in cation-deficient (V_{Cu}, V_{Zn}, and V_{Sn}) samples existed as vacancy clusters containing both cation vacancies and intrinsic Se vacancies, which induced the formation of localized disorderly oriented domains. These cation deficiencies contributed to the improved electrical conductivity and power factor of the corresponding $Cu_{2(1-x)}Zn_{1-y}Sn_{1-z}Se_4$ samples *via* an increase in the hole carrier concentration. Moreover, the induced local disordering contributed to further reduced thermal conductivity *via* stronger phonon scattering. As a result, enhanced *ZT* performance was achieved in all cation deficient samples. Among them, Sn-deficient $Cu_2ZnSnSe_4$ obtained the highest *ZT* value of 0.44 at 750 K, which was two times larger than that of pristine sample (*ZT* = 0.14 at 750 K). The cation–anion vacancy cluster and local disordered structure elucidated in the present work open up a new avenue to tackle the entanglement of thermoelectric parameters by proper vacancy modulation.

Introduction

Thermoelectric conversion technology enables an environmentally friendly conversion between heat and electricity without any moving parts and detrimental emissions, and therefore stands for a unique opportunity for the realization of green and renewable energy utilization.[1,2] However, the large-scale commercial application of the thermoelectric technology is still hindered by the scarcity of high-performance thermoelectric materials as well as mature devices based on them.[1,3,4] The performance of a thermoelectric material is evaluated by a dimensionless figure of merit *ZT* defined as $ZT = \sigma S^2 T/\kappa$, where σ is the electrical conductivity, S is the Seebeck coefficient, T is the absolute temperature (in Kelvin), and κ is the thermal conductivity.[5,6] Apparently, an ideal thermoelectric candidate should be a combination of high σ and S as well as low κ. However, these parameters are reversely coupled, which makes it quite challenging to obtain a gratifying *ZT* value and an energy-conversion efficiency that can compete with the existing power generation or refrigeration technologies in the market. Therefore, seeking new strategies and systems to disentangle the interrelated parameters from each other to further improve the *ZT* value has always been the main interests in the thermoelectric community.[7–12]

In order to acquire a high *ZT* figure of merit, thermoelectric solids usually try to interweave glass-like poor thermal properties with crystal-like good electrical properties, the so-called phonon-glass electron-crystal (PGEC) concept.[13–15] Among them, the phonon-glass behavior is usually tied to amorphous or disordered systems, which often show ultralow κ,[16,17] one of the qualifications required for high-performance thermoelectric materials. However, due to the general structural disorders, the electrical properties of above amorphous systems are also very poor,[17,18] setting up considerable obstacles to pursue a high *ZT* performance. As compared to general amorphous or disordered systems, a locally disordered crystalline materials might provide a solution to the current dilemma,[19,20] in which the rigid

[a]*Hefei National Laboratory for Physical Sciences at the Microscale, CAS Center for Excellence in Nanoscience, University of Science and Technology of China, Hefei 230026, P. R. China. E-mail: cxiao@ustc.edu.cn*

[b]*Institute of Energy, Hefei Comprehensive National Science Center, Hefei 230031, P. R. China*

[c]*Hefei National Laboratory for Physical Sciences at the Microscale, State Key Laboratory of Particle Detection and Electronics, Hefei 230026, P. R. China*

† Electronic supplementary information (ESI) available: Secondary electron and backscattered electron images, EDS spectra, element composition and mapping, HRTEM and SAED characterizations, Lorenz number. See DOI: 10.1039/d0ta09866c

crystalline lattice serves as an electrical conducting framework to realize crystal-like good electrical properties, while the local disordering scatters the heat-carrying phonons to realize glass-like poor thermal property, offering an effective approach to fulfil the concept of PGEC.[14,21,22] Therefore, it is valuable to explore new strategies to induce local disordering, and tackle the undesirable electrical–thermal coupling issue in thermoelectric materials.

Due to their structure distortion-induced intrinsic low thermal conductivity, as well as nontoxicity and abundant constituent elements, quaternary I_2–II–IV–VI_4 chalcogenides, such as Cu_2ZnSnS_4 and $Cu_2ZnSnSe_4$, were established as potential practical thermoelectric materials.[21,23–28] However, the rather large band gap (about 1.0 eV for $Cu_2ZnSnSe_4$ compared to that of traditional Bi_2Te_3 (0.16 eV)[29] and PbTe (0.32 eV)),[30] and the resulting low electrical conductivity have seriously restricted the improvement of their *ZT* values. Previous studies successfully optimized the carrier concentration and electrical conductivity mainly by adopting aliovalent substitution doping on the cationic sites, such as excessive Cu self-doping on the Zn or Sn site[26,31] and Ga/In doping on the Sn site,[27,32] but also faced a few drawbacks. Due to the similar ionic radius of constituent cations (Cu^+: 0.74 Å, Zn^{2+}: 0.74 Å, and Sn^{4+}: 0.69 Å),[33] it is quite difficult to accurately position the doping site of the extrinsic dopant, which may affect the stability of the thermoelectric performance. More importantly, due to the diversity of the valence state of constituent cations, the uncertainty of the doping site will cause the uncertainty of the doping type (donor or acceptor doping), which has a direct effect on the final *ZT* performance.[34] In this regard, acceptor-type cationic vacancies with definite doping site offer the perfect solution for improving the electrical properties of p-type I_2–II–IV–VI_4 thermoelectrics.

In the present study, we adopted cation vacancy modulation and highlighted the vacancy cluster-induced local disordered structure as an effective strategy for the significant enhancement of thermoelectric property in $Cu_2ZnSnSe_4$. By artificially creating cation deficiencies (V_{Cu}, V_{Zn}, and V_{Sn}) in the pristine lattice (as shown in Fig. 1), the combined evidences from positron annihilation and HRTEM characterizations strongly indicated that the vacancies in cation deficient samples existed as vacancy clusters containing cation vacancies and intrinsic Se vacancies, which induced the formation of local disordered domains in a macroscopically crystalline lattice. These cation vacancies contributed to an increase in the hole carrier concentration, thus improving the electrical conductivity and the power factor ($PF = \sigma S^2$) of corresponding $Cu_{2(1-x)}Zn_{1-y}Sn_{1-z}Se_4$ samples. Moreover, the vacancy cluster-induced local disordered structure was beneficial for stronger phonon scattering with further reduced thermal conductivity. As a result, improved thermoelectric performance was achieved in all three cation deficient samples. Among them, the 2 mol% Sn deficient sample reached the highest *ZT* value of 0.44 at 750 K, which was markedly enhanced by 2 times compared to that of pristine sample ($ZT = 0.14$). The cation–anion vacancy cluster and local disordered structure elucidated in present study also establish a new avenue for the exploration of high-performance thermoelectric materials by proper vacancy modulation.

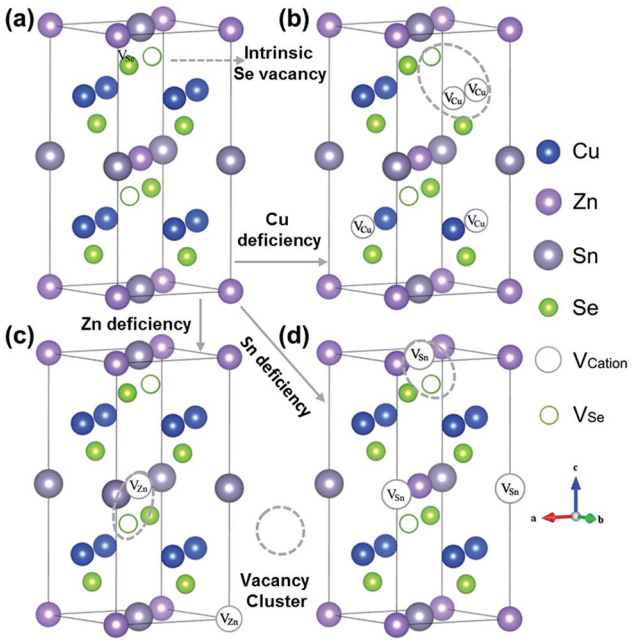

Fig. 1 Schematic representation of the crystal structure of pristine $Cu_2ZnSnSe_4$ with intrinsic Se vacancy (a) and cation deficient $Cu_2ZnSnSe_4$ with Cu (b), Zn (c), and Sn vacancy (d), respectively. The gray dotted circles indicate the possible vacancy cluster defect configuration.

Experimental

Chemicals

The starting elemental powders, including Cu (2.7 N), Sn (2.5 N), Se (CP), were purchased from Sinopharm Chemical Reagent Co., Ltd, Zn powder (4 N) was purchased from Aladdin Reagent Company. All chemicals were used as received without further purification.

Sample synthesis and sintering

Samples of pristine $Cu_2ZnSnSe_4$ and $Cu_{2(1-x)}Zn_{1-y}Sn_{1-z}Se_4$ ($x = 0.02$, $y = 0.02$, and $z = 0.02$; nominal composition) were synthesized by a vacuum solid-state reaction route. Stoichiometric mixtures of Cu, Sn, Se, and Zn powders were homogenized in an agate mortar manually for about 20 to 30 min and sealed in evacuated silica tubes with an outer diameter of 8 mm and an inner diameter of 6 mm. It was found that purer products could be obtained in shorter tubes according to the experiments. Specifically, the length of the sealing tube was shorter than 5 cm, with sample quantity about 2 mmol or total mass less than 1.5 g to prevent the quartz tube from bursting due to the excessive volatile pressure of Se. The tubes were upright placed in a "well-type" muffle furnace using a corundum crucible, and subsequently heated up to 923 K with 3 K min^{-1} heating rate, and kept at this temperature for 24 h. Then, the tubes were further heated up to 1073 K with 3 K min^{-1} heating rate and held there for another 96 h. Finally, the tubes were cooled down to room temperature at a cooling rate of 1 K min^{-1}. The as-prepared bulk products were ground into fine powder for about 20 min in an agate mortar. All sample

preparation processes, including the weighing of raw materials and grinding of powders, were carried out of air. For sample sintering, the obtained powders were hot-pressed into a disk-shaped sample (pellet) of ϕ16 mm × 2.5 mm under the axial compressive stress of 60 MPa at 723 K for 30 min *via* a vacuum hot pressing furnace (Shanghai Chen Xin Electric Furnace Co., Ltd). Before the pressure was applied, the sample was kept at that temperature for about 20 min, and the pressure was gradually removed with the decrease in temperature after hot pressing.

Structure and morphology characterizations

The structure of the samples was characterized *via* X-ray diffraction (XRD) patterns recorded on an X-ray diffraction system (Philips X' Pert PRO SUPER) using a Cu K_α source (λ = 1.5418 Å) from 10° to 70° at a scanning rate of 0.2° s^{-1}. Raman spectra were recorded by a confocal micro-Raman microscope (LabRam-HR) with the 514.5 nm wavelength for excitation. The scanning electron microscopy (SEM) images, energy dispersive spectroscopy (EDS) energy spectra and elemental surface distribution mapping were obtained by a FET Sirion200 Schottky field-emission scanning electron microscope with a 25 kV test voltage. High-resolution TEM (HRTEM) images and selected area electron diffraction (SAED) were characterized on a spherical aberration-corrected JEOL ARM-200F field-emission transmission electron microscope operating at an accelerating voltage of 200 kV. The Hall coefficient measurement was performed on a Quantum Design Physical Property Measurement System (PPMS-9T) using the van der Pauw method.

Thermoelectric properties measurements

The resulting discs had more than 90% theoretical density, determined from the geometric densities. The samples were well cut and polished with a shiny surface. Rectangular shape samples with typical sizes of 10 mm × 2 mm × 2 mm were employed to simultaneously measure the electrical conductivity σ and Seebeck coefficient S by the standard four-probe methods in He atmosphere (ULVAC-RIKO, ZEM-3) and test ranging from 300 K to 750 K. Cylindrical shape samples with typical sizes of ϕ10 nm × 2 mm were used to measure thermal diffusivity D by the laser flash method (Netzsch, LFA 457), while the specific heat C_p was determined by a differential scanning calorimeter instrument (Netzsch, DSC Q2000). Thermal conductivity κ was calculated using the equation $\kappa = D\rho C_p$ from the data of thermal diffusivity, density and specific heat. Usually, the relative uncertainties of instruments were estimated to be ±4% for electric conductivity, ±3% for Seebeck coefficient, and ±3% for thermal diffusivity.

Positron annihilation spectroscopy measurements

The positron annihilation lifetime experiments were carried out on a fast–slow coincidence ORTEC system with a time resolution of about 230 ps full width at half maximum. A 30 μCi source of ^{22}Na was sandwiched between two identical $Cu_{2(1-x)}Zn_{1-y}Sn_{1-z}Se_4$ samples with a total count of two million. A 2 × 2 × 2 supercell without structure relaxation was used to calculate the theoretic annihilation lifetime of a positron in a perfect bulk crystal or that of a positron trapped at a defect by solving the three-dimensional Kohn–Sham equation with the finite difference method based on the conventional scheme[35] and the density functional theory.[36] To obtain the positron lifetimes, the GGA (Generalized Gradient Approximation) form of the enhancement factor proposed by Barbiellini[37] was chosen.

Results and discussion

Structure and composition characterizations

$Cu_{2(1-x)}Zn_{1-y}Sn_{1-z}Se_4$ samples were obtained by the simple vacuum solid-phase sintering method. As shown in Fig. 2a, all XRD patterns of the as-synthesized $Cu_{2(1-x)}Zn_{1-y}Sn_{1-z}Se_4$ samples could be indexed to the tetragonal $Cu_2ZnSnSe_4$ (space group: $I\bar{4}2m$) with lattice parameters of $a = b$ = 5.693 Å, c = 11.333 Å (JCPDS No. 52-0868), and other weak peaks were verified as the diffraction peaks of $Cu_2ZnSnSe_4$ according to simulation results, indicating that samples were of high purity and their crystal structures were not changed after the vacancy introduction. The enlarged XRD patterns of the marked area in Fig. 2a (as shown in Fig. 2b) demonstrated that the diffraction peaks have a tendency towards higher angles, meaning the decrease of interplanar spacing in cation deficient samples, which in turn reflected that the vacancy defects were successfully created. Considering the nearly identical XRD patterns of ZnSe, Cu_2SnSe_3 and $Cu_2ZnSnSe_4$, Raman spectra were further recorded to validate the phase purity of the as-synthesized samples. As shown in Fig. 2c, compared to the reported Raman shifts of ZnSe (202 cm^{-1}, 252 cm^{-1}),[38] Cu_2SnSe_3 (180 cm^{-1}, 236 cm^{-1}, 251 cm^{-1}),[39] and $Cu_2ZnSnSe_4$ (173 cm^{-1}, 197 cm^{-1}, 231 cm^{-1}),[40] the experimental Raman spectra results were consistent with that of $Cu_2ZnSnSe_4$, confirming the high

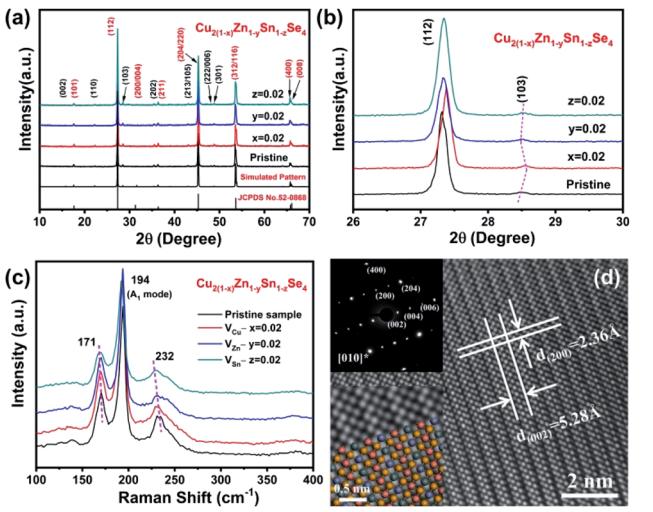

Fig. 2 Structure and phase characterization. (a) XRD patterns of the $Cu_{2(1-x)}Zn_{1-y}Sn_{1-z}Se_4$ samples. (b) The enlarged XRD patterns between 26° and 30°. (c) Raman spectra of the $Cu_{2(1-x)}Zn_{1-y}Sn_{1-z}Se_4$ samples. (d) HRTEM image of pristine $Cu_2ZnSnSe_4$ along [010] direction, with a superposition of the SAED pattern (top-left inset) and atomic structure model (bottom-left inset).

purity of the samples. Besides, a sign of phonon softening was found in cation deficient samples compared to that of pristine sample, and its degree increased from Cu-deficient to Zn-deficient, and to Sn-deficient $Cu_2ZnSnSe_4$ (as labelled by the magenta dotted line in Fig. 2c), which was related to the tendency of lattice thermal conductivity reduction.

The HRTEM image of pristine $Cu_2ZnSnSe_4$ presented in Fig. 2d with alternating light and dark lattice stripes, as well as the clear, no-splitting Bragg diffraction spots (top-left inset) all manifested the single nature of the grain. From the image, two typical crystal planes with interplanar spacing of 2.36 Å and 5.28 Å, and interplanar angle of 90° were obtained, which could be indexed to the (200) and (002) crystal planes of tetragonal $Cu_2ZnSnSe_4$. However, compared to the standard card values (No. 52-0868), some minor differences still existed between the experimental data and the theoretical data ($d_{(200)\text{theoretical}} = 2.84$ Å, $d_{(002)\text{theoretical}} = 5.67$ Å), which may be due to the intrinsic Se vacancies, as discussed below. The intrinsic Se deficiency in pristine $Cu_2ZnSnSe_4$ caused a lattice shrinkage and resulted in *d*-spacing value differences. According to the indexed planes, the HRTEM image could be easily calibrated as the [010] zone axis atom projection, whose contrast could partly reflect the relative positions of atoms. Combined with the superimposed atomic structure along the [010] direction (bottom-left inset in Fig. 2d), we could determine the corresponding atoms, and revealed the clear alternating "–Zn(Sn)–Se–Cu–Se–Sn(Zn)–Se–Cu–Se–" layers, which could match with the crystal structure, as shown in Fig. 1, further confirming the phase purity and well crystallinity of pristine $Cu_2ZnSnSe_4$.

To investigate the effect of cation deficiency on the phase and element uniformity of the samples, backscattered electron (BSE) images and elemental mapping were taken on typical polished samples. As shown in Fig. S1,† the homogeneity in contrast of the BSE images for pristine and Sn deficient $Cu_2ZnSnSe_4$ samples indicated a single, uniform phase, which was in consistence with the homogeneous element area distribution results by EDS mapping (Fig. S2†). It is worth noting that quite a lot of crystal voids (marked by red dotted circles in Fig. S1a and b†) in a μm length scale were found in both pristine and Sn deficient $Cu_2ZnSnSe_4$ samples, which is thought to be due to the volatility of Se during hot pressing.[41] The element compositions were obtained according to the EDS quantitative analysis. As shown in Table S1,† the content of Se and Sn were both obviously lower than theoretical value, which should be responsible for the lattice shrinkage mentioned above. Moreover, in cation deficient samples, the corresponding cation element showed a relative low content compared to that of pristine $Cu_2ZnSnSe_4$, which suggested that extrinsic cation vacancies were successfully introduced in the corresponding samples. These results demonstrated that all the $Cu_{2(1-x)}Zn_{1-y}Sn_{1-z}Se_4$ samples showed a single uniform phase with intrinsic Se deficiency and void defects due to the volatilization of Se.

Vacancy cluster and local disordered structure studies

To determine the effect of the extrinsic cation deficiency on the vacancy configuration in $Cu_{2(1-x)}Zn_{1-y}Sn_{1-z}Se_4$ samples, we

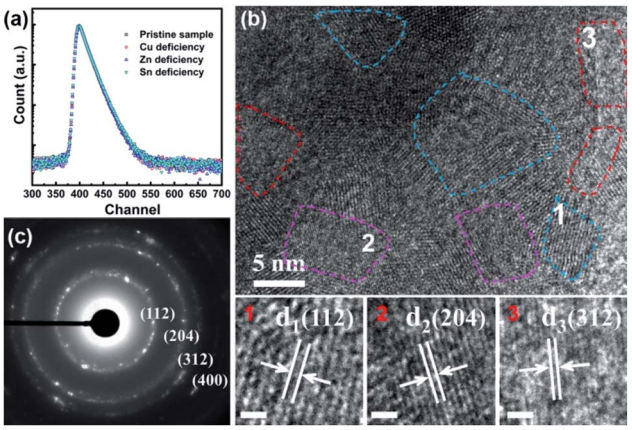

Fig. 3 Positron annihilation spectroscopy and HRTEM characterizations. (a) Positron lifetime spectrum of $Cu_{2(1-x)}Zn_{1-y}Sn_{1-z}Se_4$ samples. (b and c) HRTEM image (b) and the corresponding selected area electron diffraction (SAED) pattern (c) of a Sn-deficient $Cu_2ZnSnSe_4$ grain, showing local disordered oriented domains. Panel 1, 2, and 3 are the enlarged views of the corresponding marked areas in the HRTEM image (b), scale bar, 1 nm.

conducted positron annihilation spectroscopy (PAS) measurements to thoroughly investigate the vacancy defect in this system by virtue of its discriminating detection of vacancy-type defects (particularly those that are negatively charged) in solid materials.[42–44] As shown in Fig. 3a, the similar positron annihilation lifetime spectrum implied that there was no significant difference between the average positron lifetimes though cation vacancy was expected to induce a longer annihilation lifetime. The spectra for all samples were decomposed into two lifetime components using the LTv9 program,[45] as shown in Table 1. We can see that the lifetimes (τ_1 and τ_2) of different $Cu_{2(1-x)}Zn_{1-y}Sn_{1-z}Se_4$ samples are very similar, while their intensities (I_1 and I_2) showed obvious differences along with different cation deficiency. The shorter lifetime component (τ_1, 235–264 ps) was related to vacancy defects, while the longer lifetime component (τ_2, 416–437 ps) came from positron annihilation in the large size defects, such as voids stated above, in the samples.[43] From pristine $Cu_2ZnSnSe_4$ to Cu-deficient to Zn-deficient, and to Sn-deficient $Cu_2ZnSnSe_4$, the τ_2 component showed an increasing trend in intensity, which implied the increase concentration of large size defects.

To better understand our experimental results, the theoretical positron lifetime values of possible defects in the $Cu_2ZnSnSe_4$ system are calculated and listed in Table 2. Considering the intrinsic Se deficiency, we also accounted the

Table 1 Positron lifetime parameters of $Cu_{2(1-x)}Zn_{1-y}Sn_{1-z}Se_4$ samples

Sample	τ_1 (ps)	τ_2 (ps)	I_1 (%)	I_2 (%)
$Cu_2ZnSnSe_4$	263.8	437.4	64.5	35.5
$Cu_{2(1-0.02)}ZnSnSe_4$	251.9	429.6	62.6	37.4
$Cu_2Zn_{1-0.02}SnSe_4$	261.2	416.2	60.1	39.9
$Cu_2ZnSn_{1-0.02}Se_4$	235.1	426.9	52.3	47.7

Table 2 Calculated positron lifetime values in $Cu_2ZnSnSe_4$ System

Defect type	Bulk	V_{Cu}	V_{Zn}	V_{Sn}	V_{Se}	V_{Cu-Se}	V_{Zn-Se}	V_{Sn-Se}	V_{Se-Se}
Lifetime (ps)	228	236	236	247	243	291	290	312	257

possibility of dual-vacancies containing cation vacancy and Se vacancy. Compared to the calculated results, the τ_1 component was longer than the bulk lifetime as well as theoretical lifetimes of M mono-vacancy, but it was smaller than that of M–Se dual-vacancies (M = Cu, Zn, or Sn), which indicated that the τ_1 component was the composite lifetime of bulk and corresponding cation vacancy defect. Meanwhile, the above results also suggested that the vacancy configuration in cation-deficient $Cu_{2(1-x)}Zn_{1-y}Sn_{1-z}Se_4$ was quite complex, and vacancy clusters containing both cation vacancy and intrinsic Se vacancies may be the most possible existing defect configuration. From the perspective of the crystal structure (see Fig. 1), Se atom formed chemical bonds with all cation atoms, which also facilitated the missing of both cation and Se atoms and the formation of vacancy clusters containing both cation and Se vacancies.

Once a number of vacancy defects, particularly large-sized vacancy clusters, are induced in the lattice, it will inevitably affect the local crystal structure, for example, promoting the generation of dislocations.[46,47] In order to investigate the effect of vacancy cluster defects on the local structure of the $Cu_{2(1-x)}Zn_{1-y}Sn_{1-z}Se_4$ samples, HRTEM and selected area electron diffraction (SAED) characterizations were conducted. As shown in Fig. 2d, although having intrinsic Se vacancies, the pristine $Cu_2ZnSnSe_4$ demonstrated well single crystallinity. However, for cation-deficient $Cu_{2(1-x)}Zn_{1-y}Sn_{1-z}Se_4$, things seemed to be very different. Taking Sn-deficient $Cu_2ZnSnSe_4$ as an example, Fig. 3b and c show the HRTEM image and SAED pattern of a grain of several hundred nanometers. To our surprise, the HRTEM image manifested disordered oriented domains, which were consistent with the dispersive diffraction spots with circular profile shown by SAED pattern. As shown in Fig. 3b, the Sn-deficient $Cu_2ZnSnSe_4$ had disordered domains of several nanometers, such as (204), (112), and (312) crystal planes, corresponding to the diffraction rings in Fig. 3c. It should be noted that these crystal planes did not belong to the same zone axis, showing an amorphous character.[48–50] The Cu- and Zn-deficient $Cu_2ZnSnSe_4$ also demonstrated similar results (see Fig. S3 and S4†). These dispersive diffraction spots and disordered oriented domains unambiguously revealed that when large number of vacancies and vacancy clusters exist, cation-deficient $Cu_{2(1-x)}Zn_{1-y}Sn_{1-z}Se_4$ samples contained a special local disordered crystalline structure, which surely effected their electrical and thermal transport properties.

Electrical performance for $Cu_{2(1-x)}Zn_{1-y}Sn_{1-z}Se_4$ samples

The electrical transport properties of our $Cu_{2(1-x)}Zn_{1-y}Sn_{1-z}Se_4$ samples were measured and displayed in Fig. 4. Fig. 4a shows the temperature dependent electrical conductivity. The electrical conductivity of pristine $Cu_2ZnSnSe_4$ increased from 221

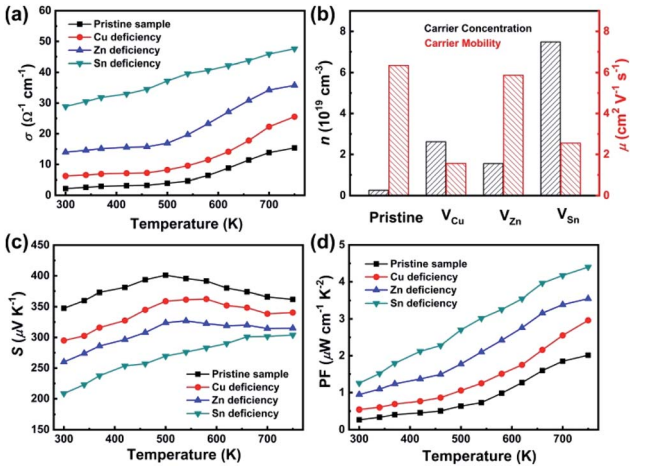

Fig. 4 Electrical transport properties. (a–d) Temperature-dependent electrical conductivity (a), room temperature carrier concentration and mobility (b), temperature-dependent Seebeck coefficient (c) and power factor (d) of the $Cu_{2(1-x)}Zn_{1-y}Sn_{1-z}Se_4$ samples.

Ω^{-1} m^{-1} at 300 K to 1536 Ω^{-1} m^{-1} at 750 K, showing a semiconductor behavior. After the introduction of cation vacancies, all cation deficient samples showed obviously increased electrical conductivity compared to that of pristine counterpart, among which Sn-deficient $Cu_2ZnSnSe_4$ reached the highest value of 4700 Ω^{-1} m^{-1} at 750 K, about 2 times larger than that of pristine $Cu_2ZnSnSe_4$. As confirmed by the Hall carrier measurement in Fig. 4b, Sn-deficient $Cu_2ZnSnSe_4$ had the highest hole concentration of 7.5×10^{19} cm^{-3} and the moderate carrier mobility at 300 K, rationalizing its highest electrical conductivity. In addition, the Zn-deficient $Cu_2ZnSnSe_4$ had very high carrier mobility compared to Cu-deficient counterpart, which led to its higher electrical conductivity. This was because the upper part of the valence bands in $Cu_2ZnSnSe_4$ were mainly composed of Cu 3d and Se 4p orbitals,[51] and therefore Cu vacancies played a bigger role in diminishing mobility rather than Zn and Sn vacancies.

Contrary to the variation trend in electrical conductivity, the Seebeck coefficients of $Cu_{2(1-x)}Zn_{1-y}Sn_{1-z}Se_4$ decreased from pristine sample to cation-deficient ones, as shown in Fig. 4c. This phenomenon can be easily understood with the increase in the hole concentration after the formation of cation vacancies. The temperature dependent Seebeck coefficient first increased monotonically at low temperatures, and then began to decrease after 500 K, except for the Sn-deficient sample, which was consistent with the sudden increase of electrical conductivity around 500 K (Fig. 4a). Due to the large band gap nature of the $Cu_2ZnSnSe_4$ materials, a bipolar contribution to this anomaly could be ignored. Thus, we speculated that the high carrier concentration may suppress a few internal variations near 500 K and cause this anomaly. Another interesting thing was that the electrical conductivity and Seebeck coefficient increased simultaneously at a low temperature range below 500 K, which was inconsistent with conventional understanding. Several studies on these quaternary I_2–II–IV–VI_4 chalcogenides also reported similar behavior.[24,52–54] The exact reason behind this

phenomenon is not clear, but we suspect that it may be probably related to change of density of sate effective mass (m^*) during the change of temperature. Combining the results from σ and S, the power factor of $Cu_{2(1-x)}Zn_{1-y}Sn_{1-z}Se_4$ was obtained (Fig. 4d). Although with opposite variation trend, the notable increase in σ after the introduction of cation vacancies compensated the decrease in S and finally improved PF. Due to its highest σ, the Sn-deficient sample kept the highest PF value among all studies samples, and doubled the performance of the pristine sample.

Thermal performance and figure of merit *ZT* for $Cu_{2(1-x)}Zn_{1-y}Sn_{1-z}Se_4$ samples

The thermal transport properties of our $Cu_{2(1-x)}Zn_{1-y}Sn_{1-z}Se_4$ samples were measured and displayed in Fig. 5. First, all samples had a relatively low thermal conductivity due to the intrinsic Se deficiency and void defects discussed above, and decreased with an increase in the temperature due to dominate Umklapp phonon–phonon scattering.[55] Moreover, upon cation vacancy modulation, the thermal conductivity could be further reduced. As shown in Fig. 5a, the temperature-dependent total thermal conductivity for $Cu_{2(1-x)}Zn_{1-y}Sn_{1-z}Se_4$ decreased from the pristine sample to Cu-deficient to Zn-deficient, and to Sn-deficient over the entire measuring temperature range, achieving a minimum value of 2.25 W m^{-1} K^{-1} at 300 K, and 0.74 W m^{-1} K^{-1} at 750 K. This decreasing trend in thermal conductivity was consistent with that of the phonon softening degree evidenced by Raman spectra (Fig. 2c), directly relating to the local disordered structure. In wide-band-gap $Cu_2ZnSnSe_4$, the thermal excitation-induced bipolar diffusion could be ignored, therefore, the total thermal conductivity κ only consisted of two parts: the electronic thermal conductivity, κ_e, and the lattice thermal conductivity, κ_l (*i.e.*, $\kappa = \kappa_e + \kappa_l$). κ_e was estimated from the Wiedemann–Franz relation,[56] $\kappa_e = L\sigma T$, where L was the Lorenz number obtained by fitting the respective Seebeck coefficient values with an estimate of the reduced chemical potential. The detailed calculation process can be found in a few published works.[12,34,57] According to the calculated L (shown in Fig. S5†), the temperature-dependent κ_e and κ_l were given in Fig. 5b and c, respectively. It can be obviously seen that the electronic part increased with an increase in the electrical conductivity and contributed very small proportion to κ. In the meantime, the additional strong phonon scattering from vacancy clusters and local disordered structure in cation-deficient samples led to further reduction in κ_l, which overwhelmed the increase in κ_e and finally optimized the total thermal conductivity κ to a very low value.

The simultaneous optimization of electrical and thermal transport properties presented above promoted the significant improvement in final thermoelectric performance. As shown in Fig. 5d, all three cation deficient samples showed increased *ZT* values as compared to its native $Cu_2ZnSnSe_4$. The highest *ZT* value of 0.44 was achieved at 750 K in the Sn-deficient sample, which was twice larger than that of pristine $Cu_2ZnSnSe_4$ and among the top values reported for bulk $Cu_2ZnSnSe_4$-based thermoelectric materials at similar temperature level (~750 K).[27,28,31,32,52] Based on the above discussion, this substantial enhancement was unambiguously correlated to the vacancy cluster and local disordered structure existed in cation-deficient samples, which optimized the carrier concentration to improve the PF and offered a phonon scattering center to further reduce the lattice thermal conductivity.

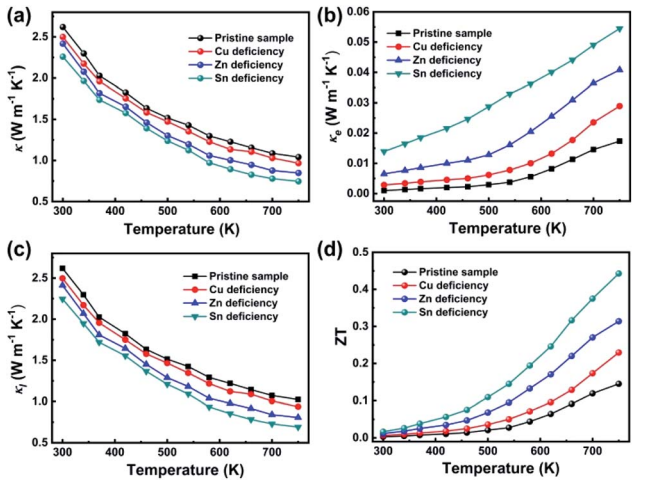

Fig. 5 Thermal transport properties and *ZT* value. (a–d) Temperature-dependent total thermal conductivity (a), electronic thermal conductivity (b), lattice thermal conductivity (c), and dimensionless thermoelectric figure of merit (*ZT*) value (d) of the $Cu_{2(1-x)}Zn_{1y}Sn_{1-z}Se_4$ samples.

Conclusions

In summary, we highlighted the local disordered crystalline structure as an effective strategy to synergistically optimize electrical and thermal properties. Guided by the idea of vacancy engineering, we investigated the effect of different types of cation deficiency (V_{Cu}, V_{Zn}, and V_{Sn}) on the thermoelectric properties of $Cu_2ZnSnSe_4$, and found a special vacancy cluster-induced local disordered structure. SEM and EDS analyses demonstrated that all samples had intrinsic Se vacancies and void-type crystal defects. More importantly, positron annihilation spectrum and HRTEM characterizations comprehensively indicated that the vacancies in cation deficient samples existed as vacancy clusters containing both cation vacancies and intrinsic Se vacancies, and led to the formation of local disordering, which increased the hole carrier concentration and offered phonon scattering center to further reduce the lattice thermal conductivity. As a result, a simultaneous optimization of the electrical and thermal conductivities was achieved, which compensated the deterioration in Seebeck coefficient, and finally improved the *ZT* performance in all three cation deficient samples. For example, 2 mol% Sn-deficient $Cu_2ZnSnSe_4$ obtained a maximum *ZT* value of 0.44 at 750 K, which was 200% higher than that of the pristine sample (~0.14 at 750 K). Although this *ZT* value is low as compared to state of art thermoelectric systems, the vacancy cluster-induced local disordered structure elucidated in present work represents a new

avenue to fulfil the "PGEC" concept, which is helpful to disentangle the undesirably coupled thermoelectric parameters.

Conflicts of interest

There are no conflicts to declare.

Acknowledgements

This work was supported by the National Key R&D Program of China (2018YFB0703602, 2017YFA0303500, and 2019YFA0210000), the National Natural Science Foundation of China (21622107, U1832142, and 21805269), the Youth Innovation Promotion Association CAS (2016392), the Fundamental Research Funds for the Central Universities (WK2340000094), the Anhui Provincial Natural Science Foundation (1808085QA08), the Key Research Program of Frontier Sciences (QYZDY-SSW-SLH011), and the China Postdoctoral Science Foundation (2017M620261).

References

1 G. Tan, L.-D. Zhao and M. G. Kanatzidis, *Chem. Rev.*, 2016, **116**, 12123–12149.
2 Y. Xiao and L. Zhao, *Science*, 2020, **367**, 1196–1197.
3 J. He and T. M. Tritt, *Science*, 2017, **357**, eaak9997.
4 X. Shi and L. Chen, *Nat. Mater.*, 2016, **15**, 691–692.
5 H. J. Goldsmid, in *CRC Handbook of Thermoelectrics*, ed. D. M. Rowe, CRC Press, Boca Raton, FL, 1995, p. 74.
6 J. R. Sootsman, D. Y. Chung and M. G. Kanatzidis, *Angew. Chem., Int. Ed.*, 2009, **48**, 8616–8639.
7 J. Mao, H. T. Zhu, Z. W. Ding, Z. H. Liu, G. A. Gamage, G. Chen and Z. F. Ren, *Science*, 2019, **365**, 495–498.
8 C. Zhao, Z. Li, T. Fan, C. Xiao and Y. Xie, *Research*, 2020, 9652749.
9 C. Chang, M. H. Wu, D. S. He, Y. L. Pei, C. F. Wu, X. F. Wu, H. L. Yu, F. Y. Zhu, K. D. Wang, Y. Chen, L. Huang, J. F. Li, J. Q. He and L. D. Zhao, *Science*, 2018, **360**, 778–783.
10 M. Hong, W. Y. Lyu, Y. Wang, J. Zou and Z. G. Chen, *J. Am. Chem. Soc.*, 2020, **142**, 2672–2681.
11 X. Zhang, Z. Bu, S. Lin, Z. Chen, W. Li and Y. Pei, *Joule*, 2020, **4**, 986–1003.
12 H. Zhu, Z. Li, C. Zhao, X. Li, J. Yang, C. Xiao and Y. Xie, *Natl. Sci. Rev.*, 2020, DOI: 10.1093/nsr/nwaa085.
13 G. A. Slack, in *CRC Handbook of Thermoelectrics*, ed. D. M. Rowe, CRC Press, Boca Raton, FL, 1995, p. 407.
14 C. Xiao, J. Xu, B. X. Cao, K. Li, M. G. Kong and Y. Xie, *J. Am. Chem. Soc.*, 2012, **134**, 7971–7977.
15 M. Beekman, D. T. Morelli and G. S. Nolas, *Nat. Mater.*, 2015, **14**, 1182–1185.
16 W. Zhou, Y. Cheng, K. Chen, G. Xie, T. Wang and G. Zhang, *Adv. Funct. Mater.*, 2020, **30**, 1903829.
17 K. Xia, P. Nan, S. Tan, Y. Wang, B. Ge, W. Zhang, S. Anand, X. Zhao, G. J. Snyder and T. Zhu, *Energy Environ. Sci.*, 2019, **12**, 1568–1574.
18 S. He, Y. Li, L. Liu, Y. Jiang, J. Feng, W. Zhu, J. Zhang, Z. Dong, Y. Deng, J. Luo, W. Zhang and G. Chen, *Sci. Adv.*, 2020, **6**, eaaz8423.
19 W. G. Zeier, Y. Pei, G. Pomrehn, T. Day, N. Hernz, C. P. Heinrich, G. J. Snyder and W. Tremel, *J. Am. Chem. Soc.*, 2013, **135**, 726–732.
20 G. J. Snyder, M. Christensen, E. Nishibori, T. Caillat and B. B. Iversen, *Nat. Mater.*, 2004, **3**, 458–463.
21 Q. Jiang, H. Yan, Y. Lin, Y. Shen, J. Yang and M. J. Reece, *J. Mater. Chem. A*, 2020, **8**, 10909–10916.
22 B. Yu, W. Liu, S. Chen, H. Wang, H. Wang, G. Chen and Z. Ren, *Nano Energy*, 2012, **1**, 472–478.
23 T. Wang, T. Huo, H. Wang and C. Wang, *Sci. China Mater.*, 2019, **63**, 8–15.
24 C. P. Heinrich, T. W. Day, W. G. Zeier, G. J. Snyder and W. Tremel, *J. Am. Chem. Soc.*, 2014, **136**, 442–448.
25 A. Ali, J. Jacob, M. I. Arshad, M. Ajaz un Nabi, A. Ashfaq, K. Mahmood, N. Amin, S. Ikram, U. Rehman, S. Hussain and K. Mehboob, *Solid State Sci.*, 2020, **103**, 106198.
26 D. Chen, Y. Zhao, Y. Chen, B. Wang, Y. Wang, J. Zhou and Z. Liang, *ACS Appl. Mater. Interfaces*, 2015, **7**, 24403–24408.
27 K. Wei, L. Beauchemin, H. Wang, W. D. Porter, J. Martin and G. S. Nolas, *J. Alloys Compd.*, 2015, **650**, 844–847.
28 F. J. Fan, Y. X. Wang, X. J. Liu, L. Wu and S. H. Yu, *Adv. Mater.*, 2012, **24**, 6158–6163.
29 T. C. Harman, B. Paris, S. E. Miller and H. L. Goering, *J. Phys. Chem. Solids*, 1957, **2**, 181–190.
30 B. L. Gelmont, T. R. Globus and A. V. Matveenko, *Solid State Commun.*, 1981, **38**, 931–934.
31 Y. Dong, H. Wang and G. S. Nolas, *Phys. Status Solidi RRL*, 2014, **8**, 61–64.
32 X. Y. Shi, F. Q. Huang, M. L. Liu and L. D. Chen, *Appl. Phys. Lett.*, 2009, **94**, 122103.
33 R. D. Shannon, *Acta Crystallogr., Sect. A: Cryst. Phys., Diffr., Theor. Gen. Crystallogr.*, 1976, **32**, 751–767.
34 K. Li, Z. Li, L. Yang, C. Xiao and Y. Xie, *Inorg. Chem.*, 2019, **58**, 9205–9212.
35 E. Boroński and R. M. Nieminen, *Phys. Rev. B: Condens. Matter Mater. Phys.*, 1986, **34**, 3820–3831.
36 W. Kohn and L. J. Sham, *Phys. Rev.*, 1965, **140**, A1133–A1138.
37 B. Barbiellini, M. J. Puska, T. Korhonen, A. Harju and R. M. Nieminen, *Phys. Rev. B: Condens. Matter Mater. Phys.*, 1996, **53**, 16201–16213.
38 G. Perna, M. Lastella, M. Ambrico and V. Capozzi, *Appl. Phys. A*, 2006, **83**, 127–130.
39 G. Marcano, C. Rincón, S. A. López, G. Sánchez Pérez, J. L. Herrera-Pérez, J. G. Mendoza-Alvarez and P. Rodríguez, *Solid State Commun.*, 2011, **151**, 84–86.
40 M. Dimitrievska, F. Oliva, M. Guc, S. Giraldo, E. Saucedo, A. Perez-Rodriguez and V. Izquierdo-Roca, *J. Mater. Chem. A*, 2019, **7**, 13293–13304.
41 Y. Gu, M. Li, Z. Zhang and Z. Sun, *Polym. Compos.*, 2010, **31**, 1562–1571.
42 B. Qin, Y. Zhang, D. Wang, Q. Zhao, B. Gu, H. Wu, H. Zhang, B. Ye, S. J. Pennycook and L. D. Zhao, *J. Am. Chem. Soc.*, 2020, **142**, 5901–5909.

43 Z. Li, C. Xiao, S. Fan, Y. Deng, W. Zhang, B. Ye and Y. Xie, *J. Am. Chem. Soc.*, 2015, **137**, 6587–6593.
44 B. Gu, Z. Li, J. Liu, H. Zhang and B. Ye, *Appl. Phys. Lett.*, 2019, **115**, 192106.
45 J. Kansy, *Nucl. Instrum. Methods Phys. Res., Sect. A*, 1996, **374**, 235–244.
46 Z. Chen, Z. Jian, W. Li, Y. Chang, B. Ge, R. Hanus, J. Yang, Y. Chen, M. Huang, G. J. Snyder and Y. Pei, *Adv. Mater.*, 2017, **29**, 1606768.
47 Z. Chen, B. Ge, W. Li, S. Lin, J. Shen, Y. Chang, R. Hanus, G. J. Snyder and Y. Pei, *Nat. Commun.*, 2017, **8**, 13828.
48 H. Wei, W. Guo, Y. Sun, Z. Yang and Y. Zhang, *Mater. Lett.*, 2010, **64**, 1424–1426.
49 S. Ji, T. Shi, X. Qiu, J. Zhang, G. Xu, C. Chen and C. Ye, *Sci. Rep.*, 2013, **3**, 2733.
50 R. A. Wibowo, W. H. Jung and K. H. Kim, *J. Phys. Chem. Solids*, 2010, **71**, 1702–1706.
51 D. Zou, G. Nie, Y. Li, Y. Xu, J. Lin, H. Zheng and J. Li, *RSC Adv.*, 2015, **5**, 24908–24914.
52 M. L. Liu, F. Q. Huang, L. D. Chen and I. W. Chen, *Appl. Phys. Lett.*, 2009, **94**, 202103.
53 M. Ibáñez, R. Zamani, A. LaLonde, D. Cadavid, W. H. Li, A. Shavel, J. Arbiol, J. R. Morante, S. Gorsse, G. J. Snyder and A. Cabot, *J. Am. Chem. Soc.*, 2012, **134**, 4060–4063.
54 W. G. Zeier, A. LaLonde, Z. M. Gibbs, C. P. Heinrich, M. Panthöfer, G. J. Snyder and W. Tremel, *J. Am. Chem. Soc.*, 2012, **134**, 7147–7154.
55 T. Zou, W. Xie, M. Widenmeyer, X. Xiao, X. Qin and A. Weidenkaff, *Rare Met.*, 2018, **37**, 290–299.
56 G. D. Mahan and M. Bartkowiak, *Appl. Phys. Lett.*, 1999, **74**, 953–954.
57 Y.-L. Pei, J. He, J.-F. Li, F. Li, Q. Liu, W. Pan, C. Barreteau, D. Berardan, N. Dragoe and L.-D. Zhao, *NPG Asia Mater.*, 2013, **5**, e47.